are shaped by the phase space structure of a classical one-dimensional periodically driven harmonic oscillator.

The stochastic web pattern depends on the shape of $E(p_x)$, whose Fourier coefficients determine the right-hand side of equation (2). By changing the SL composition, we can tailor $E(p_x)$ to realize stochastic webs with different two-dimensional tiling patterns. Consequently, our work links the electrical properties of nanostructures with the mathematical properties of tilings, including the Penrose tiling[28] that can occur in the phase space of a driven harmonic oscillator[8].

We have realized non-KAM chaos for electrons in a SL with stationary applied electric and magnetic fields that, surprisingly, act like a THz plane wave. At certain critical voltages the electron phase space is threaded by infinite stochastic webs, which delocalize the electron orbits and wavefunctions. This unique feature of non-KAM chaos reveals itself as a strong resonant enhancement of the measured current flow through the SL. Our results suggest that stochastic webs could provide an ultra-sensitive mechanism for controlling transmission through other periodic structures, including ultra-cold atoms in optical lattices[20,21,29], and photonic crystals in which a modulation of the lattice constant could bend light rays in a way analogous to the effect of **F** and **B** on the electron trajectories in the SL[30]. Non-KAM chaos, which began with theoretical work, now has an unexpected experimental realization in semiconductor physics. It provides a new method of switching with the potential for developing electronic and photonic devices that exploit the intrinsic sensitivity of chaos. □

1. Lichtenberg, A. J. & Lieberman, M. A. *Regular and Chaotic Dynamics* (Springer, New York, 1992).
2. Gutzwiller, M. C. *Chaos in Classical and Quantum Mechanics* (Springer, New York, 1990).
3. Stöckmann, H.-J. *Quantum Chaos: an Introduction* (Cambridge Univ. Press, Cambridge, 1999).
4. Berry, M. V. Quantum chaology. *Proc. R. Soc. Lond. A* **413,** 183–198 (1987).
5. Heller, E. J. Bound-state eigenfunctions of classically chaotic Hamiltonian systems—scars of periodic orbits. *Phys. Rev. Lett.* **53,** 1515–1518 (1984).
6. Chernikov, A. A., Sagdeev, R. Z., Usikov, D. A., Yu Zakharov, M. & Zaslavsky, G. M. Minimal chaos and stochastic webs. *Nature* **326,** 559–563 (1987).
7. Shlesinger, M. F., Zaslavsky, G. M. & Klafter, J. Strange kinetics. *Nature* **363,** 31–37 (1993).
8. Zaslavsky, G. M., Sagdeev, R. Z., Usikov, D. A. & Chernikov, A. A. *Weak Chaos and Quasi-Regular Patterns* (Cambridge Univ. Press, Cambridge, 1991).
9. Kamenev, D. I. & Berman, G. P. *Quantum Chaos: a Harmonic Oscillator in Monochromatic Wave* (Rinton, Princeton, New Jersey, 2000).
10. Chia, P.-K., Schmitz, L. & Conn, R. W. Stochastic ion behaviour in subharmonic and superharmonic electrostatic waves. *Phys. Plasmas* **3,** 1545–1568 (1996).
11. Karney, C. F. F. & Bers, A. Stochastic ion heating by a perpendicularly propagating electrostatic wave. *Phys. Rev. Lett.* **39,** 550–554 (1977).
12. Beloshapkin, V. V. *et al.* Chaotic streamlines in pre-turbulent states. *Nature* **337,** 133–137 (1989).
13. Gardiner, S. A., Cirac, J. I. & Zoller, P. Quantum chaos in an ion trap: the delta-kicked harmonic oscillator. *Phys. Rev. Lett.* **79,** 4790–4793 (1997).
14. Demikhovskii, V. Ya., Kamenev, D. I. & Luna-Acosta, G. A. Quantum weak chaos in a degenerate system. *Phys. Rev. E* **59,** 294–302 (1999).
15. Fromhold, T. M. *et al.* Effects of stochastic webs on chaotic electron transport in semiconductor superlattices. *Phys. Rev. Lett.* **87,** 046803 (2001).
16. Demikhovskii, V. Ya., Izrailev, F. M. & Malyshev, A. I. Manifestation of Arnol'd diffusion in quantum systems. *Phys. Rev. Lett.* **88,** 154101 (2002).
17. Jensen, R. V. Quantum chaos. *Nature* **355,** 311–318 (1992).
18. Wilkinson, P. B. *et al.* Observation of 'scarred' wavefunctions in a quantum well with chaotic electron dynamics. *Nature* **380,** 608–610 (1996).
19. Fromhold, T. M. *et al.* Tunneling spectroscopy of mixed stable-chaotic electron dynamics in a quantum well. *Phys. Rev. B* **65,** 155312 (2002).
20. Hensinger, W. K. *et al.* Dynamical tunnelling of ultra-cold atoms. *Nature* **412,** 52–55 (2001).
21. Steck, D. A., Oskay, W. H. & Raizen, M. G. Observation of chaos-assisted tunneling between islands of stability. *Science* **293,** 274–278 (2001).
22. Amann, A., Schlesner, J., Wacker, A. & Schöll, E. Chaotic front dynamics in semiconductor superlattices. *Phys. Rev. B* **65,** 193313 (2002).
23. Esaki, L. & Tsu, R. Superlattice and negative differential conductivity in semiconductors. *IBM J. Res. Dev.* **14,** 61–65 (1970).
24. Tsu, R. & Döhler, G. Hopping conduction in a "superlattice". *Phys. Rev. B* **12,** 680–686 (1975).
25. Patanè, A. *et al.* Tailoring the electronic properties of GaAs/AlAs superlattices by InAs layer insertions. *Appl. Phys. Lett.* **81,** 661–663 (2002).
26. Wacker, A. Semiconductor superlattices: a model system for nonlinear transport. *Phys. Rep.* **357,** 1–111 (2002).
27. Canali, L., Lazzarino, M., Sorba, L. & Beltram, F. Stark-cyclotron resonance in a semiconductor superlattice. *Phys. Rev. Lett.* **76,** 3618–3621 (1996).
28. Penrose, R. The role of aesthetics in pure and applied mathematical research. *Bull. Inst. Math. Appl.* **10,** 266–271 (1974).
29. Scott, R. G., Bujkiewicz, S., Fromhold, T. M., Wilkinson, P. B. & Sheard, F. W. Effects of chaotic energy-band transport on the quantized states of ultracold sodium atoms in an optical lattice with a tilted harmonic trap. *Phys. Rev. A.* **66,** 023407 (2002).
30. Wilkinson, P. B. & Fromhold, T. M. Chaotic ray dynamics in slowly varying two-dimensional photonic crystals. *Opt. Lett.* **28,** 1034–1036 (2003).

Observation of rare-earth segregation in silicon nitride ceramics at subnanometre dimensions

Naoya Shibata[1], Stephen J. Pennycook[1], Tim R. Gosnell[2], Gayle S. Painter[3], William A. Shelton[4] & Paul F. Becher[3]

[1]*Condensed Matter Sciences Division, Oak Ridge National Laboratory, Oak Ridge, Tennessee 37831, USA*
[2]*Pixon LLC, 100 North Country Road, Setauket, New York 11733, USA*
[3]*Metals and Ceramics Division, Oak Ridge National Laboratory, Oak Ridge, Tennessee 37831, USA*
[4]*Computer Science and Mathematics Division, Oak Ridge National Laboratory, Oak Ridge, Tennessee 37831, USA*

Silicon nitride (Si_3N_4) ceramics are used in numerous applications because of their superior mechanical properties[1,2]. Their intrinsically brittle nature is a critical issue, but can be overcome by introducing whisker-like microstructural features[3,4]. However, the formation of such anisotropic grains is very sensitive to the type of cations used as the sintering additives[1,2,5]. Understanding the origin of dopant effects, central to the design of high-performance Si_3N_4 ceramics, has been sought for many years. Here we show direct images of dopant atoms (La) within the nanometre-scale intergranular amorphous films typically found at grain boundaries, using aberration corrected Z-contrast scanning transmission electron microscopy. It is clearly shown that the La atoms preferentially segregate to the amorphous/crystal interfaces. First-principles calculations confirm the strong preference of La for the crystalline surfaces, which is essential for forming elongated grains and a toughened microstructure. Whereas principles of micrometre-scale structural design are currently used to improve the mechanical properties of ceramics, this work represents a step towards the atomic-level structural engineering required for the next generation of ceramics.

Brittleness is a limiting factor in the use of ceramics, so approaches to ensure high fracture resistance are actively being sought. In Si_3N_4 based ceramics[6], this can be attained through 'self-reinforced' microstructures consisting of elongated β-Si_3N_4 grains embedded in a fine-grained matrix. Analogous to whisker-reinforced ceramics, these reinforcing microstructures promote toughening mechanisms (for example, crack bridging, pull out and crack deflection), especially when combined with the appropriate interfacial strengths[7,8]. This microscopic composite concept is well in hand; however, the next generation of ceramics will need to

be designed at the atomic level to obtain the required improvements in mechanical properties and reliability. To do this, we must understand the role of interfacial interactions, particularly those involving dopant elements. Until now, our understanding of dopant/alloying effects has largely been based on empirical approaches. The present study integrates theory, atomic level characterization and experiment to resolve an important technical issue in ceramics, and take ceramic design to the atomistic scale.

The reinforcement concept is possible in Si_3N_4 because the grains typically exist as elongated hexagonal prisms; this is a result of the preferred crystal habit combined with anisotropic growth, in which the c-axis growth rate exceeds that normal to the prism faces[9]. This anisotropic grain growth behaviour is known to be markedly altered by the addition of some metal oxides, most notably the rare-earth oxides[5]. Thus, selective dopant additions offer the potential for tailoring the mechanical properties through microstructure optimization. Generally, Si_3N_4 ceramics are fabricated through liquid phase sintering, where oxynitride amorphous intergranular films (IGF) with nanometre-scale thickness are formed at grain boundaries[10]. Grain growth along the c-axis (length) direction is controlled by diffusion and is quite fast; however, diametrical

growth on the very smooth prism surfaces of the Si_3N_4 grains is typically reaction rate limited. Dopants will influence the growth process at these prism surfaces, but the mechanism has not been well understood. A limited number of studies have been conducted[11,12]; however, the atomic level details about how the dopants are distributed at the grain/matrix interface versus within the IGF have been extremely difficult to assess, owing to the very small thickness (that is, <2 nm) of the IGF and its amorphous nature.

Recent progress in aberration correction for scanning transmission electron microscopy (STEM) now offers the possibility of characterizing the detailed atomic structures in localized volumes such as the IGFs using a fine probe with a diameter of less than 1 Å (refs 13,14). In the annular dark-field (ADF)-STEM imaging method, the fine electron probe is scanned across a thin specimen, and electrons scattered by each atomic column are collected via an annular detector to form atomic-resolution images. The spatial resolution is critically dependent on the probe size, and can be greatly improved by the aberration correction[13]. Moreover, by using the ADF detector to collect scattered electrons at higher angles, the image intensities correspond directly to the atomic number (Z) of constituent atoms in the materials[15,16]. In order to investigate the dopant state within the IGF in Si_3N_4 ceramics, we have used the high-angle (HA) ADF-STEM imaging method combined with aberration correction for the probe formation. In this study, a lanthanum oxide (La_2O_3) doped β-Si_3N_4 sintered sample was selected for characterization. La_2O_3 additions are known to strongly promote anisotropic grain growth, resulting in the highest aspect ratio grains compared with other rare-earth oxides[5].

Figure 1 shows both HAADF-STEM (Fig. 1a) and bright-field (BF)-STEM (Fig. 1b) images of a typical region centred on an intergranular film, recorded simultaneously. The grain on the right in each image is aligned with the [0001] projection of β-Si_3N_4, so that the (10$\bar{1}$0) prismatic boundary plane is set at an 'edge on' condition. The grain on the left side is oriented with the (01$\bar{1}$1) planes normal to the image surface. In the HAADF-STEM image, bright spots inside the grains correspond to the Si columns, and the bright vertical band structure at the centre of the image indicates the
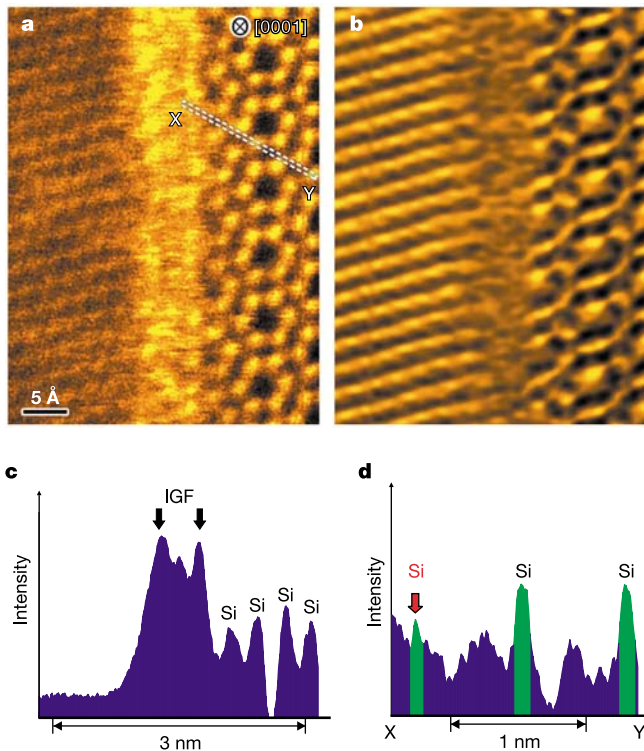
Figure 1 Atomic-resolution scanning transmission electron microscope (STEM) images of an intergranular film (IGF) in La-doped β-Si_3N_4. **a**, **b**, High-angle annular dark-field (HAADF)-STEM (**a**) and bright-field (BF)-STEM (**b**) images were simultaneously recorded at the same position. The right-hand crystal is aligned with the [0001] projection, and the left-hand crystal is oriented with the (01$\bar{1}$1) planes normal to the image surface in this condition. The bright band seen at the centre of **a** corresponds to the IGF, and brightest spots indicate the location of La atoms. **c**, The image intensity profile across the IGF summed along **a**. The image intensity is higher at the IGF than in the grain interiors, but an intensity variation can be also seen within the film. The interfaces between IGF and grains have much higher intensities than inside the IGF, indicating the preferential segregation of La to the grain surfaces. **d**, The intensity line profile across X–Y, from the edge of the IGF to the grain interior, as defined in **a**. The two green intensity peaks on the right-hand side correspond to the Si columns in the Si_3N_4 lattice. An intensity peak (indicated by the red arrow) is also found that corresponds to the Si column at the edge of the IGF. The intensity here is weaker than that of Si columns in the grain interior, suggesting that the Si column at the edge is not perfect but distorted or partially occupied along the projected direction.
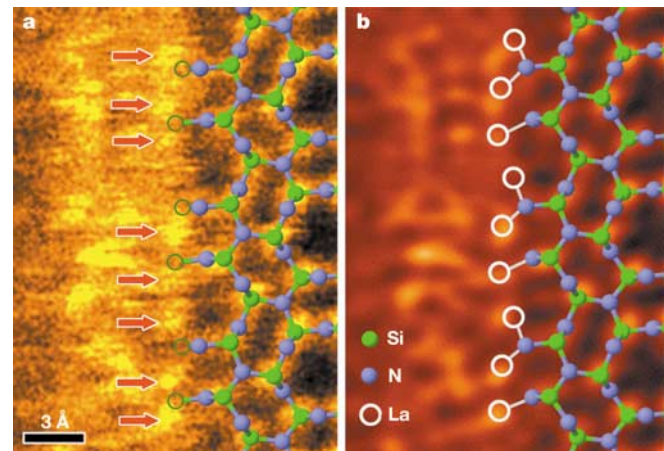
Figure 2 Magnified HAADF-STEM images of the interface between the IGF and the prismatic surface of an β-Si_3N_4 grain. The β-Si_3N_4 lattice structure is superimposed on the images. **a**, La atoms are observed as the bright spots (denoted by red arrows) at the edge of the IGF. The positions of La atoms are shifted from that of Si atoms based on the extension of the β-Si_3N_4 lattice structure; these expected positions are shown by open green circles. **b**, The Pixon (http://www.pixon.com) reconstructed image of **a**, showing the La segregation sites more clearly. The predicted La segregation sites obtained by the first-principles calculations are shown by the open white circles. These theoretical predictions agree well with the experimental result. The slight deviations (<1 Å) from some of the theoretically predicted sites probably indicate the influence of atoms in the IGF.

position of the IGF, which is confirmed by the amorphous-like contrast in the BF-STEM image of the same region. The estimated IGF thickness is about 1 nm in both images. The strong bright contrast in the IGF is due to the presence of atoms with high atomic number, in this case, La ($Z = 57$). STEM-electron energy-loss spectroscopy (EELS) spectra also confirmed the presence of La within the intergranular film. Notice that the very strong intensity in the HAADF image is observed at the IGF/grain interfaces and a minimum occurs around the centre of the IGF. Figure 1c shows the image intensity profile across the boundary taken across the width of Fig. 1a. It is clearly seen that the maximum image intensities appear at both IGF/crystalline interfaces, resulting in a bimodal intensity distribution across the IGF. The strong image intensity zone along the right edge of the IGF is located where the terminal Si columns in the right-hand grain would have existed, suggesting that this zone represents the first cation layer attached to the β-Si_3N_4 terminating surface. This is consistent with the prismatic surface of β-Si_3N_4 being terminated by a nitrogen plane, and the cations in the IGF being bonded to it forming the strong image intensity layer.

Figure 2a is a magnified HAADF-STEM image of the IGF/ prismatic crystalline interface. The β-Si_3N_4 lattice structure is superimposed on the image. At the strong intensity interfacial zone, La atoms are readily observed as bright spots (denoted by red arrows). Note that the positions of the La atoms are shifted from that of Si atoms based on the extension of the β-Si_3N_4 structure; these expected positions are shown by open green circles. The bright spots within the interfacial zone typically occur at greater distances from nearby N on the terminal grain surface than the expected Si positions, suggesting that La has a larger stable bond length than Si. On the other hand, the expected Si sites also have weaker, but definite, image intensities. The occupancy of these Si sites at the edge of the IGF was confirmed via the intensity profile taken along the white dashed line (X–Y) in Fig. 1a, as shown in Fig. 1d. This line scan runs from the edge of the IGF into the bulk β-Si_3N_4 aligned with the periodic Si columns in the grain. The periodic strong green intensity peaks represent the position of Si columns in the bulk. As indicated by the red arrow, an intensity peak is also found at the very edge of the IGF, near the extended Si position of the lattice. The intensity is weaker than that of Si columns in the bulk crystal, indicating that the column is not perfect, but distorted by the amorphous film or only partially occupied by Si along the projected direction. The same tendency is observed everywhere along the interface. This indicates that the strong image intensity zone at the edge of the IGF is formed by both La and Si atoms.

First-principles atomic cluster calculations[17] were carried out to determine the details of the stable adsorption sites and the energies of La versus Si using a N-terminated Si_3N_4 surface cluster model. To predict the stable La sites, prismatic surface cluster models with La attached were constructed, and then the structures were relaxed to allow the La atoms to reach their stable positions. As information about the precise structure of the amorphous film is lacking, we assumed a bare N-terminated surface model in this study. It was found that there are three independent stable La sites (defined by local energy minima) per surface unit cell along the N-terminated prismatic planes. Calculations show that these La sites have binding energies 0.5–5.3 eV higher than Si at its most stable surface site. Moreover, the La–N bonds are longer than comparable Si–N bonds by about 0.34–0.48 Å. Theoretically predicted stable La sites are superimposed (open white circles) on the Pixon (http://www.pix-on.com) reconstructed image shown in Fig. 2b. The reconstructed image clearly shows the strong intensity cation sites at the IGF/ crystal interface. Despite the assumption of a bare surface, the observed and predicted La positions exhibit remarkable agreement, indicating the validity of the present calculations.

The enhancement of anisotropic grain growth by La_2O_3 additions[5] must derive from preferential segregation[18] that sup-

presses diametrical growth involving the prismatic surfaces. The present results clearly show that the suppressed growth originates from the preferential segregation (and strong bonding) of La atoms to the grain surfaces; that is, the La atoms partially reside in cation sites normally available for Si at the grain surfaces, effectively hindering the Si attachment necessary for the growth reaction. The present findings provide an atomic level view of where the dopant La atoms prefer to reside in the material, and how they control the microstructure development. These results are consistent with recent first-principles (local density) calculations on the surface segregation of the rare earths competing with Si in Si_3N_4 based ceramics[18]. Differential binding energy, which differentiates rare-earth versus Si segregation strengths in environments of variable O/N ratios, was devised to distinguish the elements that remain largely bound within the amorphous phase from those that preferentially segregate to the Si_3N_4 grain surfaces (for example, La). Excellent correlation exists between the calculated differential binding energy values and measured diametric/length grain growth ratios for a variety of rare-earth elements, confirming the importance of the grain growth controlling mechanism induced by the preferential dopant segregation. We believe that the ability to combine atomistic simulations with direct atomic-scale observations of dopant atoms should significantly assist the development of structural ceramic materials. □

Methods

Atomic-resolution images were taken with a dedicated 300-kV (VG Microscopes, HB603U) scanning transmission electron microscope equipped with aberration corrector (Nion Co.), providing a minimum probe diameter of less than 1 Å. The probe convergence semiangle is approximately 22 mrad, and the HAADF image was recorded with detector angle ranges of about 35–300 mrad. The specimen for STEM observations was prepared as follows. The bulk material was mechanically polished to be about 50 μm in thickness using a precision polishing system (Allied High Tech Products, Inc., TechPrep), and then dimpled (Gatan Inc., Model 656) to have a thickness less than 10 μm before ion thinning. In the ion thinning process (Gatan Inc., Model 691), the initial accelerating voltage of Ar ions was 4.5 kV with an incident beam angle of 7°, and gradually decreased to 2 kV as thinning progressed. Finally, a low voltage ion thinning (1 kV) was applied to remove any surface damage layers (Fischione Instruments Inc., Model 1010). Thin amorphous carbon film (<3 nm) was deposited on the sample to avoid charging effects.

1. Chen, I. W., Becher, P. F., Mitomo, M., Petzow, G. & Yen, T.-S. (eds) *Silicon Nitride Ceramics—Scientific and Technological Advances* (MRS Proceedings, Mater. Res. Soc. 287, Pittsburgh, Pennsylvania, 1993).
2. Hoffmann, M. J. & Petzow, G. (eds) *Tailoring of Mechanical Properties of Si_3N_4 Ceramics* (NATO ASI Series E, Applied Sciences Vol. 276, Kluwer Academic, Dordrecht, 1994).
3. Lange, F. F. Relation between strength, fracture energy, and microstructure of hot pressed Si_3N_4. *J. Am. Ceram. Soc.* **56,** 518–522 (1973).
4. Tani, E., Umebayashi, K., Kishi, K. & Kobayashi, K. Gas-pressure sintering of Si_3N_4 with concurrent addition of Al_2O_3 and 5wt% rare earth oxide: High fracture toughness Si_3N_4 with fiber-like structure. *Am. Ceram. Soc. Bull* **65,** 1311–1315 (1986).
5. Hoffmann, M. J., Gu, H. & Cannon, R. M. in *Interfacial Engineering for Optimized Properties II* (eds Carter, C. B., Hall, E. L., Briant, C. L. & Nutt, S.) 65–74 (MRS Proceedings 586, Mater. Res. Soc., Warrendale, Pennsylvania, 2000).
6. Becher, P. F. *et al.* Microstructural design of silicon nitride with improved fracture toughness: I, Effects of grain shape and size. *J. Am. Ceram. Soc.* **81,** 2821–2830 (1998).
7. Sun, E. Y. *et al.* Microstructural design of silicon nitride with improved fracture toughness: II, Effects of yttria and alumina additives. *J. Am. Ceram. Soc.* **81,** 2831–2840 (1998).
8. Sun, E. Y. *et al.* Debonding behavior between β-Si_3N_4 whiskers and oxynitride glasses with or without an epitaxial β-SiAlON interface layer. *Acta Mater.* **47,** 2777–2785 (1999).
9. Krämer, M., Hoffmann, M. J. & Petzow, G. Grain growth studies of silicon nitride dispersed in an oxynitride glass. *J. Am. Ceram. Soc.* **76,** 2778–2784 (1993).
10. Kleebe, H.-J. Structure and chemistry of interfaces in Si_3N_4 ceramics studied by transmission electron microscopy. *J. Ceram. Soc. Jpn* **105,** 453–475 (1997).
11. Gu, H., Pan, X., Cannon, R. M. & Rühle, M. Dopant distribution in grain-boundary films in calcia-doped silicon nitride ceramics. *J. Am. Ceram. Soc.* **81,** 3125–3135 (1998).
12. Ziegler, A., Kisielowski, C., Hoffmann, M. J. & Ritchie, R. O. Atomic resolution transmission electron microscopy of the intergranular structure of a Y_2O_3-containing silicon nitride ceramic. *J. Am. Ceram. Soc.* **86,** 1777–1785 (2003).
13. Batson, P. E., Dellby, N. & Krivanek, O. L. Sub-ångstrom resolution using aberration corrected electron optics. *Nature* **418,** 617–620 (2002).
14. Krivanek, O. L., Nellist, P. D., Dellby, N., Murfitt, M. F. & Szilagyi, Z. Towards sub-0.5 angstrom electron beams. *Ultramicroscopy* **96,** 229–237 (2003).
15. Pennycook, S. J. & Jesson, D. E. High-resolution Z-contrast imaging of crystals. *Ultramicroscopy* **37,** 14–38 (1991).
16. Pennycook, S. J. Structure determination through Z-contrast microscopy. *Adv. Imag. Electron Phys.* **123,** 173–206 (2002).

17. Averill, F. W. & Painter, G. S. Symmetrized partial-wave method for density functional cluster calculations. *Phys. Rev. B* **50,** 7262–7267 (1994).
18. Painter, G. S., Becher, P. F., Shelton, W. A., Satet, R. L. & Hoffmann, M. J. Differential binding energies: effects of rare-earth additions on grain growth of β-Si₃N₄ and ceramic microstructure. *Phys. Rev. Lett.* submitted.

....

Predictability of El Niño over the past 148 years

Dake Chen[1,2], **Mark A. Cane**[1], **Alexey Kaplan**[1], **Stephen E. Zebiak**[1] **& Daji Huang**[2]

[1]*Lamont-Doherty Earth Observatory of Columbia University, Palisades, New York 10964, USA*
[2]*Laboratory of Ocean Dynamic Processes and Satellite Oceanography, State Oceanic Administration, Hangzhou, China*

....

Forecasts of El Niño climate events are routinely provided and distributed, but the limits of El Niño predictability are still the subject of debate. Some recent studies suggest that the predictability is largely limited by the effects of high-frequency atmospheric 'noise'[1–7], whereas others emphasize limitations arising from the growth of initial errors in model simulations[8–10]. Here we present retrospective forecasts of the interannual climate fluctuations in the tropical Pacific Ocean for the period 1857 to 2003, using a coupled ocean–atmosphere model. The model successfully predicts all prominent El Niño events within this period at lead times of up to two years. Our analysis suggests that the evolution of El Niño is controlled to a larger degree by

self-sustaining internal dynamics than by stochastic forcing. Model-based prediction of El Niño therefore depends more on the initial conditions than on unpredictable atmospheric noise. We conclude that throughout the past century, El Niño has been more predictable than previously envisaged.

Present estimates of El Niño's predictability are mostly based on retrospective predictions for the last two or three decades, encompassing a relatively small number of events[8–11]. With so few degrees of freedom, the statistical significance of such estimates is questionable. In principle, predictability can also be estimated by perturbing initial conditions in numerical model experiments, but the answer is model dependent, and existing models have not been shown to be realistic enough for this purpose. El Niño is evident in instrumental observations dating back to the mid-nineteenth century and in proxy data sets over much longer periods, but no successful attempt to 'hindcast' the historic El Niño events before the mid-twentieth century has been reported. This is due partly to the lack of adequate data for model initialization and partly to the inability of present models to make effective use of available data. The study reported here represents the first (to our knowledge) retrospective forecast experiment spanning the past one-and-a-half centuries, using only reconstructed sea surface temperature (SST) data[12] for model initialization.

The intrinsic predictability of El Niño is surely limited, but there has been much debate about what the limitations really are[1,13,14]. Classic theories consider El Niño and the Southern Oscillation (ENSO) as a self-sustaining interannual fluctuation in the tropical Pacific[15,16], being chaotic yet deterministic[17,18]. Thus its predictability is largely limited by the growth of initial errors, and the potential forecast lead time is likely to be of the order of years[8,10,19]. On the other hand, some recent studies emphasize the importance of atmospheric noise[2–4], particularly the so-called westerly wind bursts in the western equatorial Pacific[5–7]. In such a scenario, ENSO is a damped oscillation sustained by stochastic forcing, and its predictability is more limited by noise than by initial errors. This implies that most El Niño events are essentially unpredictable at long lead times, because their development is often accompanied by high-frequency forcing. Such a view is not supported by the present findings.

The observed and predicted SST anomalies averaged in the central equatorial Pacific are shown in Fig. 1a. (See Methods section
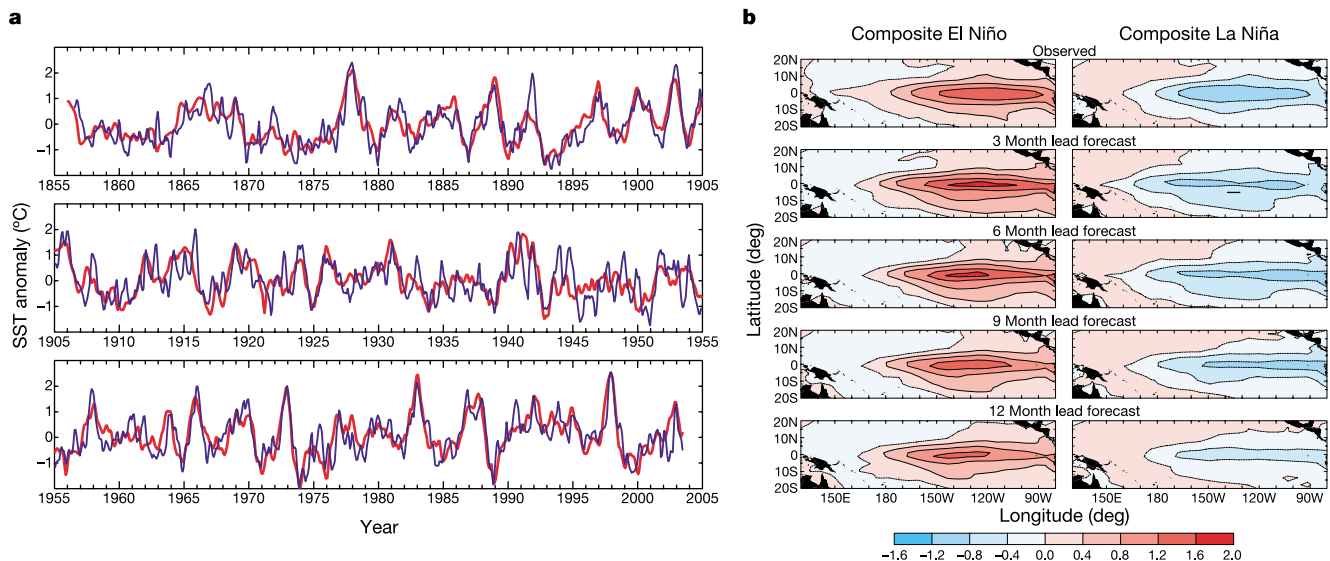
Figure 1 Retrospective predictions of El Niño and La Niña in the past 148 yr. **a,** Time series of SST anomalies averaged in the NINO3.4 region (5° S–5° N, 120–170° W). The red curve is monthly analysis of ref. 12 and the blue curve is the LDEO5 prediction at 6-month lead. **b,** Composite El Niño and La Niña from 24 warm events and 23 cold events. Top panels are observations, and the rest are predictions at different lead times. The colour bar shows the range of SST anomalies in degrees Celsius.